A 9-season TRMM Observation of the Austral Summer MJO
and Low-frequency Equatorial Waves

Hirohiko MASUNAGA

Hydrospheric Atmospheric Research Center, Nagoya University, Nagoya, Japan

(Manuscript received 18 June 2008, in final form 28 October 2008)

Abstract

A long-term observation from the Tropical Rainfall Measuring Mission (TRMM) is analyzed to investigate the Madden-Julian Oscillation (MJO), Kelvin wave, and equatorial Rossby (ER) wave in austral summer seasons. TRMM Precipitation Radar (PR) and Visible/Infrared Scanner (VIRS) measurements are jointly used to clarify convective progression associated with individual modes of the tropical oscillations. Variability in the dynamic and thermodynamic environment involving sea surface temperature (SST), column relative humidity (CRH), and moisture convergence is also examined. A sea surface warming is found to precede the peak MJO convection by ~10 days, while a prior SST increase is not as evident for the Kelvin and ER waves. Moisture convergence and CRH exhibit a horseshoe-like pattern in the composite MJO map, constituted of a pair of off-equatorial maxima and a weak equatorial peak. The Kelvin wave has a moist anomaly on the equator leading the convective peak as theoretically expected, while the moist anomaly also extends poleward without being accompanied by moisture convergence. Moisture convergence leads CRH by a day or two for the Kelvin and ER waves. Moisture convergence is, in contrast, virtually concurrent with CRH for the MJO. The correlation between CRH and deep stratiform coverage is diverse among the three modes of the tropical oscillations. Shallow cumulus and cumulus congestus lead the MJO convective peak by ~1 day, followed by lingering non-precipitating high clouds. ER wave convection is led by moisture convergence but lagged by CRH. The convective progression appears not to proceed in a monotonic way for the ER wave.

A possible mechanism to explain MJO propagation is discussed as suggested by a synthesis of the present findings. The Kelvin wave guides the eastward migration of MJO convection onset over the Indian Ocean. The role of the Kelvin wave in MJO propagation diminishes as the MJO enters the west Pacific with the convective area shifting away from the equator. Instead, the Kelvin wave convective heating induces poleward moisture transport and moistens the off-equatorial mid troposphere. The resultant moist anomaly is hypothesized to help trigger the MJO convective burst upon the arrival of ER wave disturbances. Such cooperative processes involving the Kelvin and ER waves could act as a driving engine of some, if not all, MJO episodes.

1. Introduction

A family of tropical clouds contains a rich variety of convective systems ranging over a broad spectrum from shallow cumulus to cumulonimbus. The regional

Corresponding author: Hirohiko Masunaga, Hydrospheric Atmospheric Research Center, Nagoya University, Furocho, Chikusa-ku, Nagoya 464-8601, Japan
E-mail: masunaga@hyarc.nagoya-u.ac.jp

gradient of tropical cloud population often shows a pattern related to large-scale circulations, where deep (shallow) systems prevail under an ascending (descending) branch of the circulation. Besides such climatological regionality, various types of clouds are often observed to be organized together in individual meteorological disturbances. A classical example is mesoscale convective systems (MCSs), where deep convective cores are typically accompanied by shallower cumulus on the leading edge as well as trailing stratiform precipitation. A similar pattern of

convective progression has been also documented in association with convectively coupled equatorial waves. Notable examples are the quasi 2-day wave (Takayabu et al. 1996), Kelvin wave (Straub and Kiladis 2003a), and intraseasonal oscillations (Lin and Johnson 1996; Kiladis et al. 2005; Morita et al. 2006). Mapes et al. (2006) analyzed in situ measurement data and cloud resolving model outputs to test the hypotheses explaining the coherent development of convection observed across a wide range of spatial and temporal scales. Haertel et al. (2008) investigated the heating profiles and the corresponding variation of convective clouds in terms of their thermodynamic roles in large-scale waves. A long-term, wide-area observations have yet to be analyzed for obtaining robust climatological evidence beyond the reach of a field campaign, in particular for studying synoptic- and planetary-scale disturbances. The present paper explores convective variability associated with large-scale tropical oscillations on the basis primarily of satellite data analysis.

Satellite measurements have been often utilized for detecting different modes of convectively-coupled equatorial waves. Many studies were carried out with infrared imagery (Takayabu 1994; Wheeler and Kiladis 1999; Wheeler et al. 2000; Roundy and Frank 2004; Masunaga 2007) while some used direct precipitation measurements (Cho et al. 2004; Masunaga et al. 2006). Little attempt, however, has been made to distinguishably identify the individual convective families such as shallow cumulus and cumulonimbus associated with the observed equatorial waves. Shallow clouds are difficult to isolate in infrared satellite images, because cloud tops are so warm that they are virtually indiscernible from the background thermal radiation. Optically thick clouds with cold tops are distinctly observable, whereas infrared radiation has no sensitivity to the in-cloud structure shielded by the cloud top. A breakthrough was brought by the Tropical Rainfall Measuring Mission (TRMM) Precipitation Radar (PR). The TRMM PR, capable of profiling the vertical precipitation structure, has been proved to be useful for illustrating the global climatology of shallow precipitation as well as more developed systems with higher radar-echo tops (Short and Nakamura 2000). The TRMM PR, however, is less sensitive to frozen hydrometeors than to rain drops of the same size, so that a considerable amount of ice particles aloft could be left undetected (Masunaga et al. 2002). Exploiting radar and infrared measurements complementarily, Masunaga et al.

(2005) proposed a simple scheme to classify tropical precipitating clouds. The four "storm categories" of shallow, cumulus congestus, deep stratiform, and deep convective systems were identified in terms of PR echo-top height and TRMM Visible/Infrared Scanner (VIRS) infrared brightness temperature (IR T_b) (Masunaga et al. 2005; Masunaga and Kummerow 2006). The present analysis follows their storm categorization scheme.

The study target is three modes of the tropical low-frequency oscillations, i.e., the Madden-Julian Oscillation or MJO (Madden and Julian 1972), Kelvin wave, and $n = 1$ equatorial Rossby (ER) wave coupled with moist convection[1]. The current analysis is focused on these particular modes for two major purposes. First, TRMM PR measurements are impractical for studying high-frequency waves such as the mixed Rossby-gravity wave and inertio-gravity waves. The PR swath sweeps only ~1/4 of the tropical band on daily basis, so that the high-frequency modes are difficult to sample. The second purpose is to investigate the potential roles of the Kelvin and ER waves in the MJO driving mechanism as suggested by Masunaga et al. (2006). Masunaga et al. (2006), analyzing 10 MJO events recorded in early observations from the TRMM, found that the MJO often accompanies a group of Kelvin wave packets and intruding ER wave disturbances. They discussed the hypothesis that interactions between the Kelvin and ER waves might explain aspects of the propagation mechanism of the MJO convective envelope. The proposed mechanism was further explored by Masunaga (2007), analyzing a 25-yr record of observed outgoing longwave radiation (OLR) and reanalysis datasets. The present study tests and elaborates the hypothesis by exploiting a decadal dataset of the TRMM-observed precipitating clouds and thermodynamic environment. The study period is nine seasons of austral summer starting from late 1998. Austral summer is chosen because it is known to be the season when the MJO is most outstanding (e.g., Madden 1986). We prefer to focus on the single season rather than including the entire period of time, in order not to let meaningful signals washed out by averaging the opposite phases of seasonality together.

The datasets used for this work are described in Section 2. Convective variability and the thermodynamic environment is examined by a lagged composite analysis in Section 3. Relationships among

---

1 These three modes are hereafter called 'the tropical oscillations' wherever mentioned collectively.

different types of convective clouds and the environmental parameters are explored in terms of the spatial correlation among the lagged composite diagrams (Section 4). The results are discussed and concluded in Section 5.

2. Data

The TRMM version-6 standard products are adopted for detecting precipitating clouds. PR echo-top height is estimated from 2A25 radar reflectivity profiles. In earlier work (Masunaga et al. 2005; Masunaga and Kummerow 2006), PR echo-top height was taken from the PR storm height provided by the TRMM 2A23 product. The 2A23 storm height, however, depends on the minimum detectable echo of the PR, which decreased by ~1 dBZ when the TRMM orbit was changed in August 2001 from 350 km to 402 km in altitude. In the present study, PR echo-top height is directly computed as the altitude of the highest PR range bin that contains detectable echo. Similarly to the 2A23 storm height, three or more consecutive bins are required to have detectable radar echoes when the echo-top height is determined. The minimum detectable reflectivity is defined here as 19 dBZ, which is applied uniformly throughout the periods before and after the satellite orbital change.

VIRS infrared brightness temperature is obtained from the channel-4 (10.8 μm) radiance in the TRMM 1B01 product. The PR and VIRS footprints are matched up on a quarter-degree global grid, where only the nearest neighbors to each grid point are selected. In the matchup procedure, multiple VIRS footprints are averaged together with a two-dimensional Gaussian weight corresponding to the PR beam pattern, in attempt to mitigate the discrepancy in spatial resolution between the sensors. VIRS measurements falling outside the narrower PR swath are discarded. The TRMM data of every 15–16 orbits are jointly mapped in a daily dataset.

Shallow, cumulus congestus, deep stratiform, and deep convective systems are separately identified from PR echo-top height and VIRS infrared brightness temperature (T_b) (Table 1). The definitions are equivalent to those proposed by Masunaga et al. (2005) except for the shallow category. The constraint on infrared radiance ($T_b > 260$ K) originally imposed to shallow cumulus has been removed so that low-level clouds overlapped with high clouds are allowed to join the shallow category. This revision leads to a distinct increase of the shallow cloud coverage in convectively active regions, where shallow cumulus is frequently

Table 1. Definition of storm categories.

Storm category	PR echo-top height	IR T_b
Shallow	<4 km	
Cumulus congestus	4-6 km	>245 K
Deep stratiform	4-6 km	<245 K
Deep convective	>6 km	<245 K
Non-precipitating high cloud	no rain	<245 K

overcast by detrained cirrus clouds. An additional category of non-precipitating high clouds is also considered in this work. Non-precipitating high clouds are defined to have cloud tops as cold as the deep stratiform and deep convective categories ($T_b < 245$ K) but are required not to have detectable PR echo.

Sea surface temperature (SST) and precipitable water (PW) are obtained from the TRMM Microwave Imager (TMI) datasets provided by Remote Sensing Systems. Column relative humidity (CRH), or PW normalized by saturation water vapor path, is used as the measure of tropospheric moisture. Bretherton et al. (2004) found that CRH is more directly related to precipitation than PW across all tropical oceans. PW retrieved by the TMI is used to compute CRH. The TMI-estimated PW is also used to compute moisture convergence, assuming that a substantial portion of tropospheric water vapor lies within the planetary boundary layer (PBL):

$$\int \nabla \cdot (\rho q_v \boldsymbol{v}) dz \approx \nabla \cdot \left(\boldsymbol{v}_{\mathrm{PBL}} \int \rho q_v dz \right)$$
$$= \nabla \cdot (\boldsymbol{v}_{\mathrm{PBL}} \, \mathrm{PW}), \qquad (1)$$

where p, q_v, $\boldsymbol{v}$, and z are the dry-air density, vapor mixing ratio, horizontal velocity vector, and vertical coordinate, respectively. The horizontal velocity within the PBL, $\boldsymbol{v}_{\mathrm{PBL}}$, is replaced with $\boldsymbol{v}$ at 1000 hPa, taken from the National Center for Environmental Prediction (NCEP)/National Center for Atmospheric Research (NCAR) Reanalysis daily dataset. Altering the 1000 hPa level to 925 hPa for the definition of $\boldsymbol{v}_{\mathrm{PBL}}$ was found to introduce no notable change to the geographical pattern of moisture convergence. Air temperature is also adopted from the NCEP/NCAR Reanalysis data for calculating the saturation water vapor to define CRH.

The contribution of free-tropospheric humidity to moisture convergence is not precisely taken into account in the approximate formula above (Eq. 1).
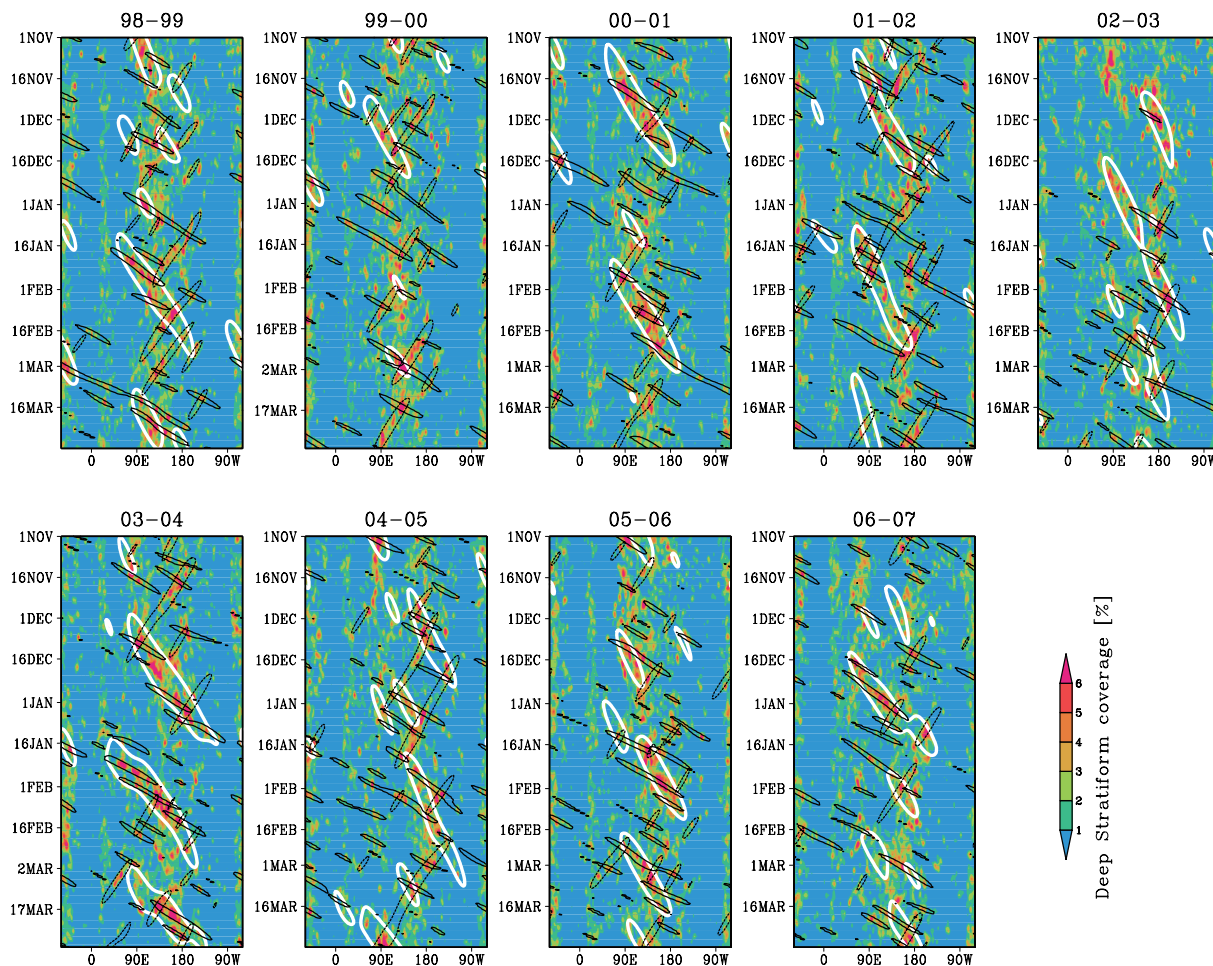
Fig. 1.   Time-longitude diagrams of 5-month (from November to March) sequences for 9 consecutive years as indicated at the top of each panel. Color shade illustrates deep stratiform coverage, smoothed by three passes of the 1-2-1 filter applied temporally and spatially. MJO-filtered deep stratiform coverage is indicated by white contour drawn at +0.5% in anomaly. The Kelvin and ER waves are contoured in black at +0.65%, where the eastward-propagating (westward-propagating) component represents the Kelvin (ER) wave.

This simplification has been examined for validity in comparison with another estimate of moisture convergence, calculated strictly from the vertical profiles of humidity and horizontal wind in the NCEP/NCAR reanalysis dataset. Qualitative patterns in composite and correlation diagrams presented later were found very insensitive to the way how moisture convergence is calculated (not shown). On the other hand, the "exact" moisture convergence is considerably weaker in magnitude than the approximate moisture convergence given by Eq. (1). Although the approximate formula might possibly exaggerate the magnitude of moisture convergence to some extent, the negative bias in amplitude is presumably because tropical moisture variability tends to be underestimated in the NCEP/NCAR reanalysis data (Trenberth and Guillemot 1998). We therefore prefer to employ observationally determined humidity for defining moisture convergence at the expense of potential higher-order errors introduced by the simplification.

3. Composite horizontal structure

3.1   Filtering and compositing methods

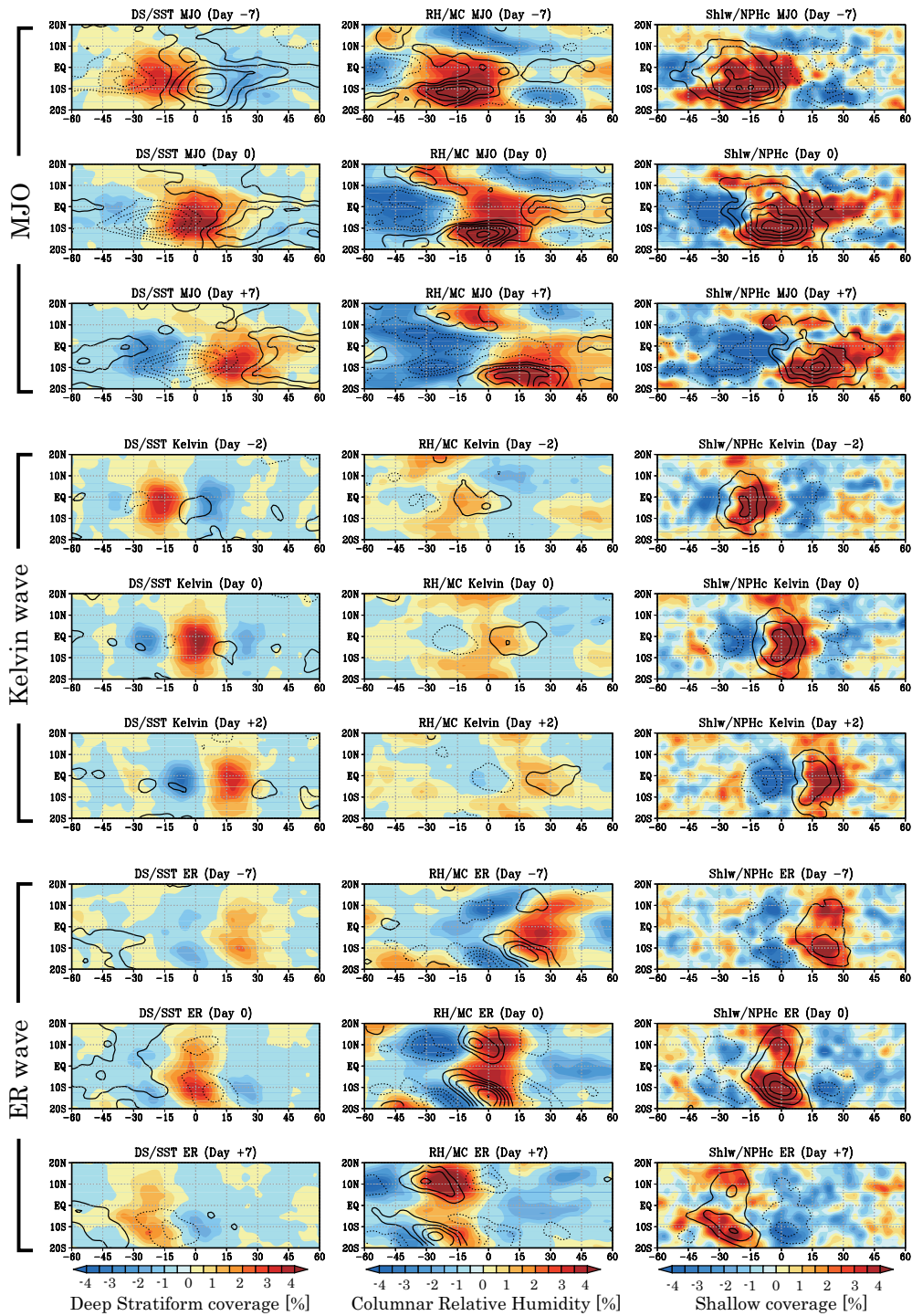Wheeler and Kiladis (1999) devised a technique to

Fig. 2. Lagged composite diagrams for the MJO (top 3 rows), the Kelvin wave (middle 3 rows), and the ER wave (bottom 3 rows). Lag is labelled on the top of each panel. *Left column*: Deep stratiform coverage (shaded) and SST (contoured at 1 K intervals with negative anomalies dashed). *Middle column*: CRH (shaded) and moisture convergence (contoured at 2×10^{-5} kg m^{-2} s^{-1} intervals with negative anomalies dashed). *Right column*: Shallow cumulus coverage (shaded) and non-precipitating high cloud coverage (contoured at 2% intervals with negative anomalies dashed).

isolate different modes of convectivelycoupled equatorial wave by applying space-time bandpass filters to outgoing longwave radiation (OLR) data. Masunaga et al. (2006) slightly modified their method to distill the tropical oscillations from TRMM observations. The Masunaga et al. (2006) scheme, adopted in this study with minor revisions, is outlined as follows. The area coverage of deep stratiform systems (hereafter denoted by deep stratiform coverage) is first calculated and averaged over each $1.25° \times 1.25°$ grid box. Deep stratiform coverage is used as an index of convective activity throughout this paper because mature convective systems often accompany extensive stratiform precipitation. The daily global maps of deep stratiform coverage are then integrated along meridian over 20°S–20°N. Narrowing the meridional coverage was found not to introduce any qualitative change to the overall pattern in the time-longitude space. Although TRMM PR overpasses do not entirely cover the globe for a single day, missing data are all complemented when grid boxes are accumulated meridionally. Bandpass filters are then applied to the time-longitude section of deep stratiform coverage. The MJO filter is defined as $1 \leq k \leq 7$, 0.0125 cpd $\leq \omega \leq$ 0.05 cpd (20–80 days in period), where k and ω are zonal wavenumber and frequency, respectively. The Kelvin-wave filter is bounded by $1 \leq k \leq 10$, 0.05 cpd $\leq \omega \leq$ 0.25 cpd (4–20 days in period), and a pair of theoretical dispersion relations with the equivalent depths of 5 m and 100 m. The $n = 1$ ER-wave filter is defined between $-10 \leq k < 0$ and two dispersion relations with the same pair of equivalent depths.

The 10-year sequence of TRMM observation from 1998 to 2007 is divided into three separate periods: *I*) January 1, 1998 to August 6, 2001 (1314 days), *II*) August 23, 2001 to September 4, 2002 (378 days), and *III*) October 18, 2002 to December 31, 2007 (1901 days). The gaps between consecutive periods are due to the TRMM orbital change in August 2001 and a temporary shutoff of the VIRS instrument from September to October 2002. Filtering analysis does not allow a gap to exist in the data, and is performed with the three periods of time separately.

Figure 1 shows the filtered MJO, Kelvin wave, and ER wave as well as the original field of deep stratiform coverage for 5-month sequences from November to March. Note that a first few months of the 2002–03 season is not properly filtered because these months are so close to the beginning of the period *II* that signals are lost by the data tapering. The overall pattern is as expected from similar filtering analyses

in the literature (e.g., Wheeler and Weickmann 2001). Major MJO episodes extending from the Indian Ocean (~60°E) to the east of the dateline are observed typically once or twice every season. Some earliest MJO events for the season start in November (e.g., the 2000-01 season) and the last events can be as late as near the end of March (e.g., 2003–04). In the present paper, austral summer is defined as the five months from November to March so that all major MJO events of the season are included in the analysis. The Kelvin and ER waves are observed ubiquitously except over the African and South American continents (~30°E and ~100°W). Convectively coupled equatorial waves are known to weaken generally over a landmass (e.g., Masunaga 2007). The composite and correlation analyses performed below are applied only to oceanic scenes.

Convective variability and the associated environmental field are composited in a way similar to the scheme developed by Masunaga et al. (2006) and Masunaga (2007). The base point for the composite analysis is zonally movable along the ridge and trough of the bandpass-filtered deep storm coverage (Fig. 1). The ridge is defined as the local maximum of a filtered wave that exceeds twice the standard deviation (2σ) in amplitude. Similarly, the trough is identified as the local minimum lower than -2σ. The ridge and trough are used for compositing the wet (or convectively active) and dry (or inactive) phases of the tropical oscillations, respectively. The background field, present regardless of phases of the tropical oscillations, is then eliminated by subtracting the dry phase composite from the wet phase composite. The total numbers of the base points used in the current analysis are listed in Table 2.

The parameters to be composited are the anomalies of SST, CRH, moisture convergence, and the area coverages of shallow, cumulus congestus, deep stratiform, and deep convective systems. The TRMM-retrieved parameters, particularly those from PR measurements, do not fill a daily longitude-latitude map as mentioned earlier. In addition, the TMI-retrieved SST and PW are not available within heavily

Table 2. Statistics of composite base points for the wet phase and for the dry phase (numbers in parenthesis).

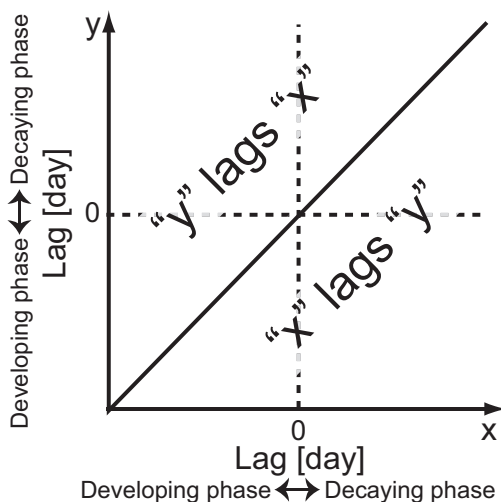|	MJO	Kelvin wave	ER wave
Global Oceans	837 (846)	1506 (1307)	1544 (1446)
Indian Ocean	170 (190)	261 (190)	226 (185)
West Pacific	296 (319)	421 (422)	510 (568)

Fig. 3.   Schematic illustration of a lagged correlation diagram, where the correlation coefficient between the variables *x* and *y* is shown for different lags with respect to the convective peak. The variable *y* (*x*) lags the other in the domain above (below) the diagonal line. Negative and positive lags correspond to the developing and decaying phases, respectively, of the tropical oscillation.

precipitating scenes. While appreciable areas could be devoid of observation in instantaneous snapshots, portions without data compensate each other when projected together on the composite plane.

The composite analysis is performed for different daily lags. Zero longitude at lag 0 corresponds by definition to where and when the tropical oscillation peaks in convective activity, and is hereafter called the convective peak.

3.2   Lagged composite diagram

Figure 2 shows lagged composite diagrams calculated over the whole tropical oceans (20°S–20°N). The left column illustrates the composite SST and convective variability. While a convective area slowly migrates to the east in association with the MJO (top 3 panels of the left column), sea surface warms up in prior to the convective peak and cools down afterward. An increase in SST leading MJO convection has been well recognized by past observational studies (Nakazawa 1995; Zhang 1996; Hendon and Glick 1997; Kemball-Cook and Weare 2001; Benedict and Randall 2007, among others). The amplitude of deep

stratiform coverage and SST is greater in the southern hemisphere than in the northern hemisphere, since the current analysis is focused on austral summer events. The MJO-composited humidity distribution (CRH) exhibits a horseshoe-like structure extending across the equator (top 3 panels in the middle column). Composite moisture convergence has a remarkable anomaly around 10°S or even further south, roughly collocated with the CRH maximum. A weaker but distinct anomaly is observed at the other end of the horseshoe in the northern hemisphere. The meridional asymmetry in amplitude is again due to the season studied in this study. The third peak, fainter than the first two, of moisture convergence anomaly lies on the equator to the east of the MJO convection peak (i.e., at a positive longitude).

Shallow cumulus composited with the MJO (top 3 panels in the right column) exhibits a horseshoe pattern similar to CRH and moisture convergence, although shallow cumulus suffers from small-scale fluctuations. The small-scale noise implies that shallow cumulus is not as tightly coupled with the MJO dynamics as deep stratiform systems. The frequency of shallow cumulus occurrence is known to be less sensitive to climatological large-scale circulation than deep convective and stratiform systems (Masunaga and Kummerow 2006). The area coverage of non-precipitating high clouds closely follows the composite spatial distribution of deep stratiform coverage. A majority of the detected non-precipitating high clouds are likely cirrus anvils accompanying MJO convection. Shallow clouds lie to the east of non-precipitating high clouds near the equator, implying that shallow cumulus leads cirrus clouds.

The SST variation associated with the Kelvin wave is far less clear (middle 3 rows of Fig. 2) than seen above with the MJO. Deep stratiform coverage is roughly symmetric about the equator, consistent with the theoretical expectation for the Kelvin wave (Matsuno 1966). CRH and moisture convergence are considerably weaker in magnitude for the Kelvin wave than for the MJO. The day-0 composite diagram nevertheless shows evidence for a moistening (drying) to the east (west) of the Kelvin wave convective peak, as originally theorized by Wang (1988) and Wang and Rui (1990). A moisture development has been observed to occur within a few days before Kelvin wave convection peaks (Straub and Kiladis 2003a). A close examination reveals that moisture convergence is centered slightly to the east of CRH. This implies that moisture convergence leads CRH for
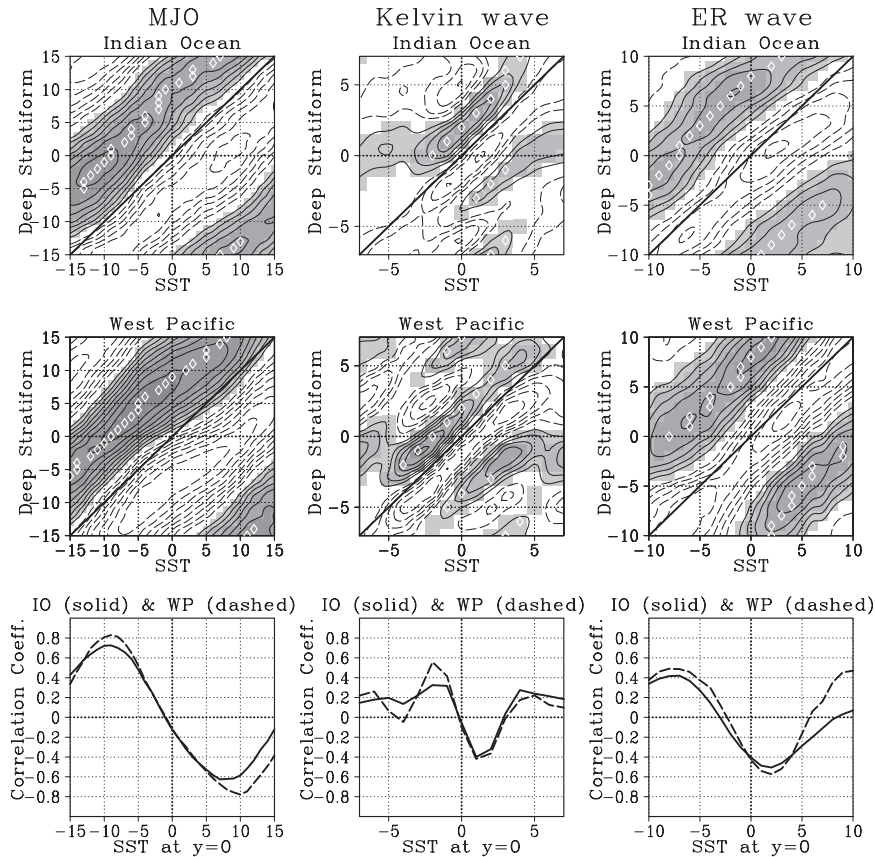
Fig. 4.   Correlation coefficients between SST (abscissa) and deep stratiform coverage (ordinate) estimated from the lagged composite diagram for the MJO (right), Kelvin wave (middle), and ER wave (left). Numbers labelled on each axis refer to lags in day with respect to the convective peak (see Fig. 3). Solid (dashed) contour, drawn at intervals of 0.1, shows positive (negative) correlation. Areas of positive correlation with statistical significance levels of 99% or higher are shaded. Diamonds indicate the location of the maximum correlation along every horizontal slice of the diagram. The horizontal slice at $y = 0$ (or day 0 in deep stratiform coverage) is delineated in the bottom row. The study region is indicated at the top of each panel.

the Kelvin wave as will become clearer in the lagged correlation analysis (Section 4). The composite CRH structure has off-equatorial wings extending to the north and south from the equatorial peak, somewhat reminiscent of the horseshoe pattern identified for the MJO. No corresponding pattern is recognizable in moisture convergence. This topic will be revisited later in Section 5.1. Shallow and nonprecipitating high clouds resemble deep stratiform systems in composite structure except for the small-scale fluctuations present in shallow cumulus coverage. A subtle eastward displacement of shallow clouds relative to non-precipitating high clouds is again barely present, although the displacement is much less apparent than seen for the MJO.

The $n = 1$ ER wave is characterized by a pair of gyres, one in each hemisphere, symmetric about the equator (Matsuno 1966). This basic structure is visually confirmed in the composite ER wave (bottom 3 rows of Fig. 2), although the meridional asymmetry in amplitude is clear here again. The sign of a preceding sea surface warming is absent or barely recognized as is the case with the Kelvin wave. On the other hand, composite maps at days 0 and +7 each show a slight eastward shift of negative SST anomaly relative to deep stratiform coverage, indicative of a surface cooling slightly lagging the convective peak. The ER wave is comparable to the MJO, and much greater than the Kelvin wave, in the amplitudes of composite CRH and moisture convergence. The paired
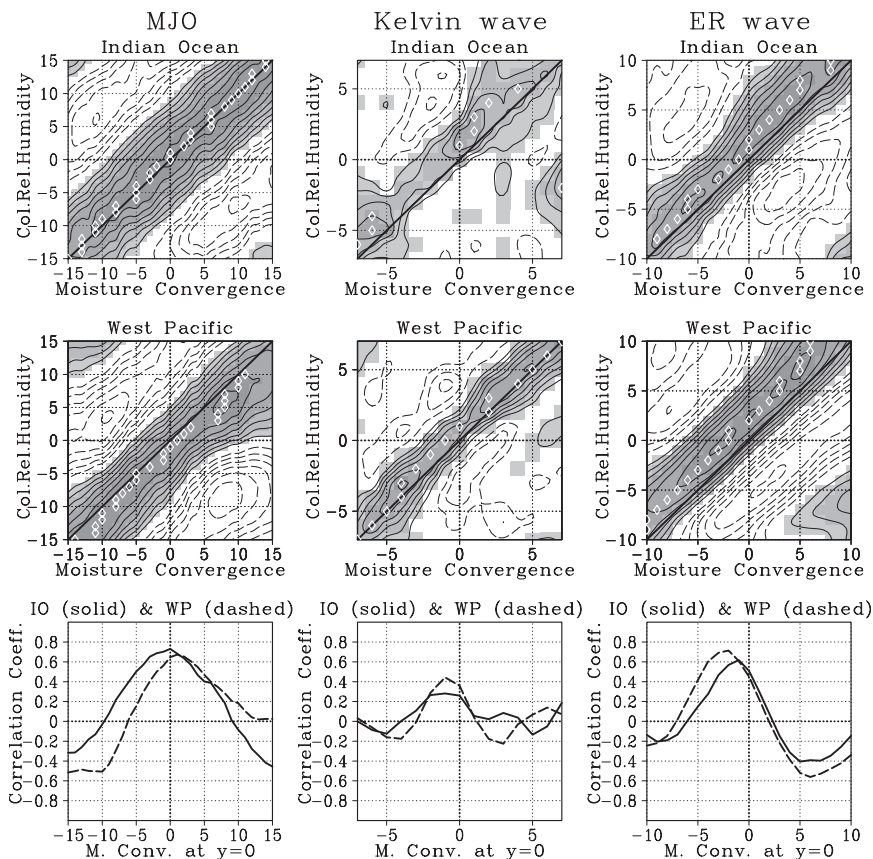
Fig. 5.   Same as Fig. 4 but for the correlation between moisture convergence and CRH.

Rossby gyres are tilted meridionally. The meridional tilt is not explained by the shallow water theory with no background flow, but is likely to exist in the presence of mean flow vertical shear (Xie and Wang 1996). Moisture convergence is similar to CRH in pattern but is shifted westward in phase, indicative of that moisture convergence leads CRH. The composite patterns of shallow and non-precipitating high clouds are overall analogous with those of deep stratiform coverage.

4.   Lagged correlation analysis

The results from the lagged composite analysis imply close relationships between the different parameters examined, sometimes with a distinct lag, in association with the tropical oscillations. Such relationships are further investigated in a quantitative manner based on a lagged correlation analysis. Results are demonstrated following a brief description on the analysis method.

4.1   Method

The spatial correlation between given two parameters, denoted by x and y, is calculated from the composite anomaly fields as shown by Fig. 2. The composite domain zonally bound between $\pm45°$ is taken into account for computing correlation coefficients. This calculation is repeated over different combinations of lags with respect to the convective peak for a given pair of parameters. One obtains $n \times n$ correlation coefficients in total, where n is the number of lags considered. The correlation coefficients are then mapped on a twodimensional plane as schematically illustrated by Fig. 3. The diagonal line partitions the lagged correlation diagram into the regions where x lags y and where y lags x. Day 0 on the abscissa and ordinate represents the convective peak of the tropical oscillation as defined in Fig. 2. Negative and positive lags correspond to the convectively developing and decaying phases, respectively.

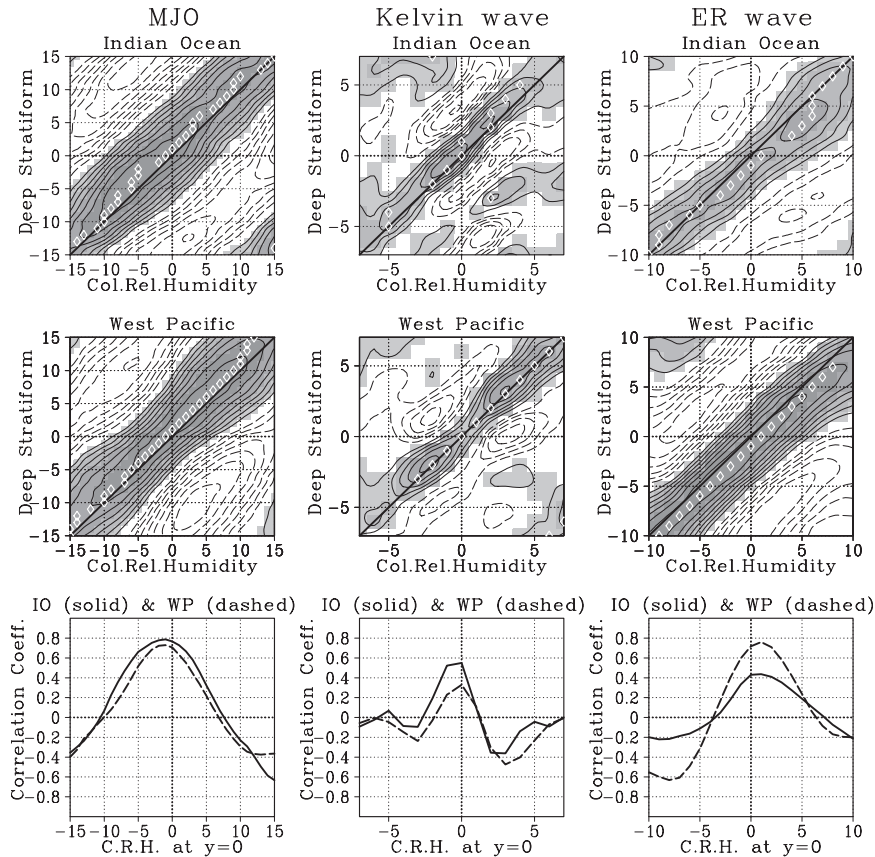The nature of convective development and decay

Fig. 6.   Same as Fig. 4 but for the correlation between CRH and deep stratiform coverage.

associated with the tropical oscillations is influenced by regionality. The convective onset of the MJO occurs in the Indian Ocean, while MJO convection matures typically over the west Pacific warm pool. The study area is therefore broken down into two major oceanic regions in order to separate the regional properties of convective variability. The current lagged correlation analysis is focused on the Indian Ocean (45°E–105°E and 20°S–20°N) and the west Pacific Ocean (120°E–180°E and 20°S–20°N) with islands and continents excluded. These definitions apply to the location of compositing base points: regions outside the designated area are therefore included when the base point is in the vicinity of the regional boundaries.

4.2   Results

a.   Sea surface temperature

Figure 4 shows the correlation between SST and deep stratiform coverage. A lag of deep stratiform coverage behind SST by about 10 days is consistent throughout the MJO life cycle in both the Indian and west Pacific Oceans. There is, however, a difference between the two oceans in the timing when the correlation is maximized. The correlation is highest when deep stratiform coverage is in its peak activity (i.e., $y = 0$) in the Indian Ocean. This confirms that a prior surface warming has a close connection to the development of MJO convection. The magnitude of correlation gradually decreases from the developing phase to the decaying phase along the "ridge" of the correlation pattern. In contrast, the correlation stays high along the ridge extending beyond 5 days or more after the convective peak in the west Pacific. It follows that, once the MJO enters the west Pacific, a sea surface cooling during the convectively active phase (Fig. 2) is linked to the subsequent decay of MJO convection as much as the preceding warming is to the convective development.

A positive correlation with SST is present but relatively weak for the Kelvin and ER waves, as we
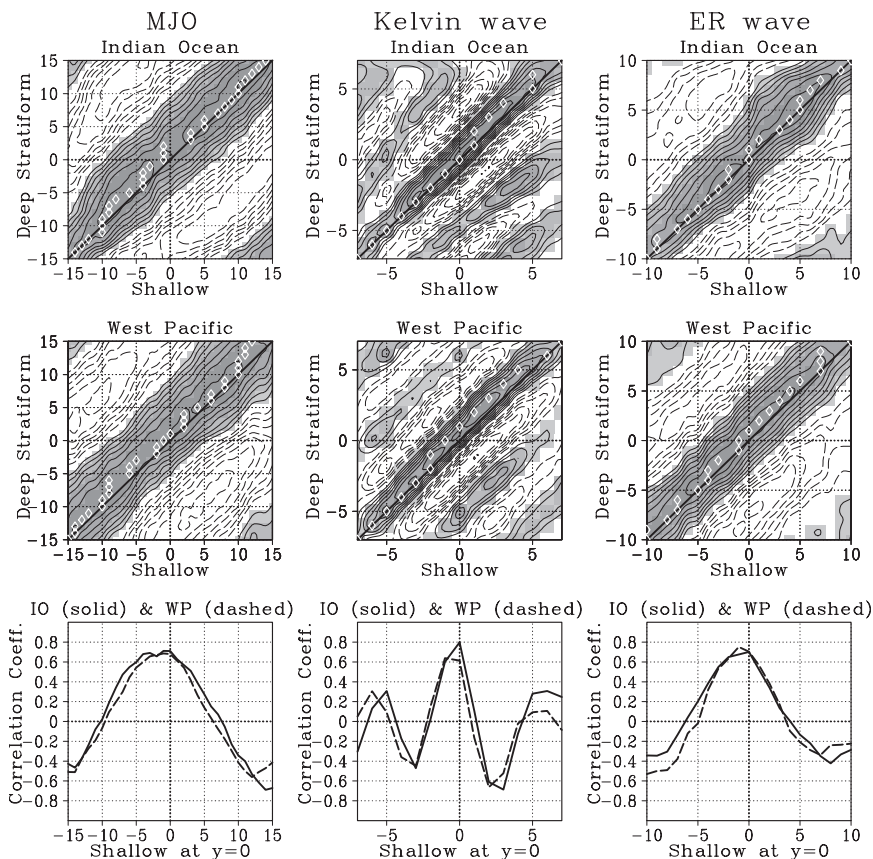
Fig. 7.   Same as Fig. 4 but for the correlation between shallow and deep stratiform coverages.

have seen in the composite diagram (Fig. 2). SST varies roughly in quadrature with MJO and Kelvin wave convections (see bottom panels of Fig. 4), whereas the oscillatory period is quite different between the MJO and Kelvin wave. The SST variation is nearly 180° out of phase, aside from a 2-day lag, with ER wave convection. A surface cooling anomaly takes the place of the prior warming as early as a few days before the ER wave convective peak.

b. Moisture convergence and column relative humidity

The correlation between moisture convergence and CRH is drawn in Fig. 5. CRH lags moisture convergence by ~1 day for the Kelvin wave. The CRH lag can be as much as 2 days for the ER wave particularly when it travels over the west Pacific. In contrast, no sign of a moisture convergence leading CRH is found for the MJO. CRH even slightly precedes moisture convergence for the MJO over the west Pacific. Past studies (Hendon and Salby 1994; Jones and Weare

1996; Maloney and Hartmann 1998; Kiladis et al. 2005) implied the presence of moisture convergence (or boundary-layer convergence) leading MJO convection. This is seemingly contrary to the present result with regard to the MJO. The existing analyses, however, focus exclusively on the equatorial convergence peak as we found to the east of (i.e., in prior to) MJO convection in Fig. 2. The contribution of the equatorial convergence peak is washed out in the current correlation analysis because the off-equatorial moisture convergence largely dominates the equatorial component in amplitude. Given the faintness of the equatorial convergence anomaly, the role of frictional moisture convergence associated with the MJO in a way postulated in the literature may need to be reconsidered. This issue will be discussed in Section 5.3.

The correlation diagram between CRH and deep stratiform coverage is depicted by Fig. 6. An one-day lag behind CRH is observed throughout the MJO
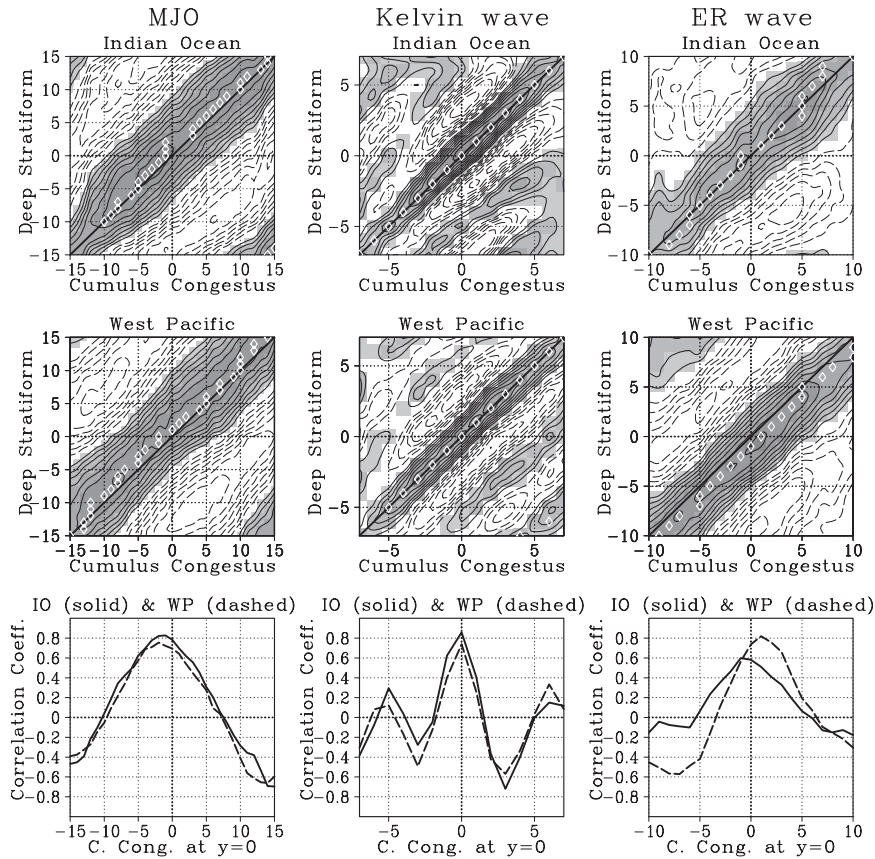
Fig. 8. Same as Fig. 4 but for the correlation between cumulus congestus and deep stratiform coverages.

cycle, although the correlation curve is approximately symmetric in time about lag 0. The lag is virtually absent in the Kelvin wave. Somewhat puzzling is that deep stratiform coverage leads CRH by a day or the ER wave. The ER wave shows a heavily skewed correlation curve.

c. Convective variability

The progression of convective clouds associated with the tropical oscillations is next explored. The lagged correlation diagram between shallow and deep stratiform coverages (Fig. 7) indicates that the area with positive correlations extends slightly wider toward the upper-diagonal domain from the $y = x$ line than to the lower-diagonal. This temporal asymmetry is present over the MJO cycle except for early days of the developing phase (lag < -10) in the Indian Ocean, i.e., a stage before the preceding SST warming. The Kelvin and ER waves also show a small lead of shallow cumulus, although not as consistently as the MJO. Straub and Kiladis (2002) found that it takes only a half day for organized convection to develop from shallow cumulus during a passage of the Kelvin wave. The dataset analyzed in the current work does not have a sufficient temporal resolution to clearly detect any phenomena changing at sub-daily time scales.

Cumulus congestus resembles shallow cumulus in the correlation diagram (Fig. 8) for the MJO. No lead or lag of cumulus congestus is identified for the Kelvin wave. Not readily expected is the fact that cumulus congestus *lags* deep stratiform systems associated with the west Pacific ER wave. Deep convective systems are precisely in phase with deep stratiform systems for all the tropical oscillations, except that a subtle delay of deep stratiform systems is barely recognizable for the Indian Ocean MJO (Fig. 9). This result does not necessarily deny a few-day lag between stratiform and convective rains during the MJO mature phase (Lin et al. 2004). The analysis by Morita et al. (2006) showed
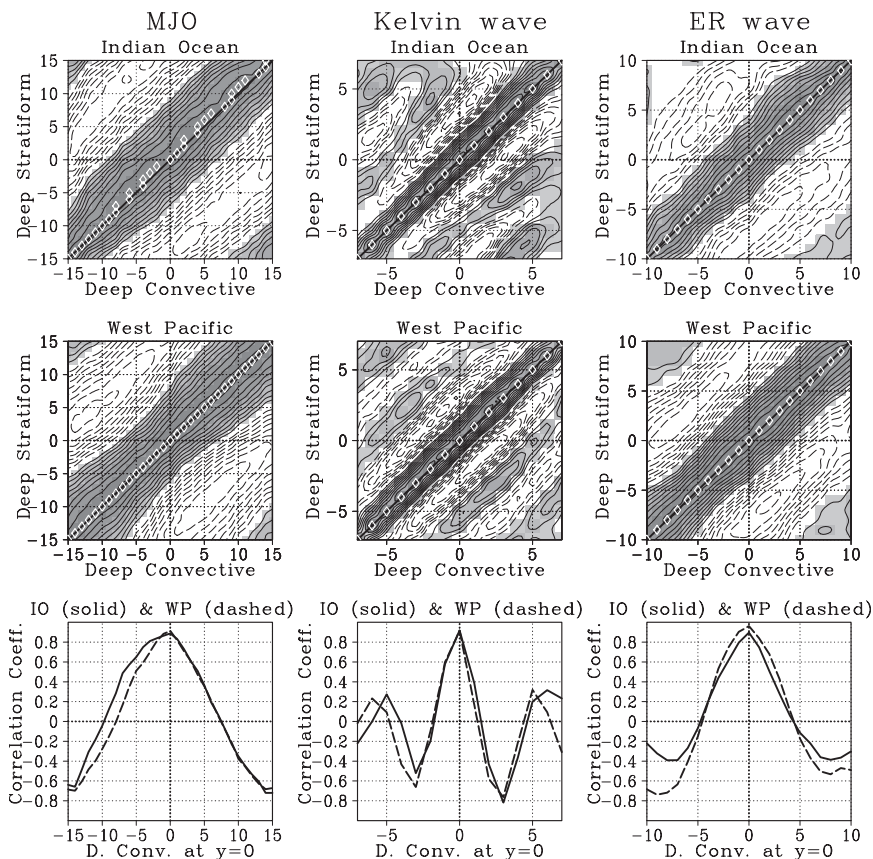
Fig. 9.   Same as Fig. 4 but for the correlation between deep convective and deep stratiform coverages.

that convective and stratiform rains composited with the MJO vary almost in phase (their Fig. 5) while stratiform rain has a long tail of weakly precipitating area extended to the west (their Fig. 6). The signal of trailing stratiform precipitation is so weak compared to intensive rainfall at the convective peak that it is perhaps not well detectable by correlation analysis as conducted here.

Finally, Fig. 10 illustrates the lagged correlation of non-precipitating high clouds with deep stratiform coverage. Non-precipitating high clouds associated with the MJO shows a lag not longer than one day, suggestive of lingering high clouds detrained from deep convective systems. The lag is physically limited to ~1 day, given the lifetime of detrainment cirrus of 30 ± 16 h (Luo and Rossow 2004). The Kelvin and ER waves show no sign of lingering high clouds.

5. Concluding discussion

In the present work the variability of convection and

relevant environmental parameters associated with the tropical oscillations has been analyzed primarily from TRMM satellite observations. A synthesis of the current findings is presented in this section for individual modes of the tropical oscillations studied.

5.1 Kelvin wave

A visual inspection of the composite and correlation diagrams (Figs. 2 and 9) suggests that dominant modes of the Kelvin wave have a zonal wavenumber of 6–8 and a period of 5–6 days. This combination of k and ω implies the equivalent depths of 10–25 m, as expected for the convectively coupled equatorial waves (Takayabu 1994; Wheeler and Kiladis 1999). The SST variation leading convection by 90° out of phase is present but faint. A preceding SST increase is explained by strong insolation under the clear-sky condition, while the subsequent surface cooling can be brought by the enhanced evaporation, developing ocean mixing layer, and/or the cloud shielding of
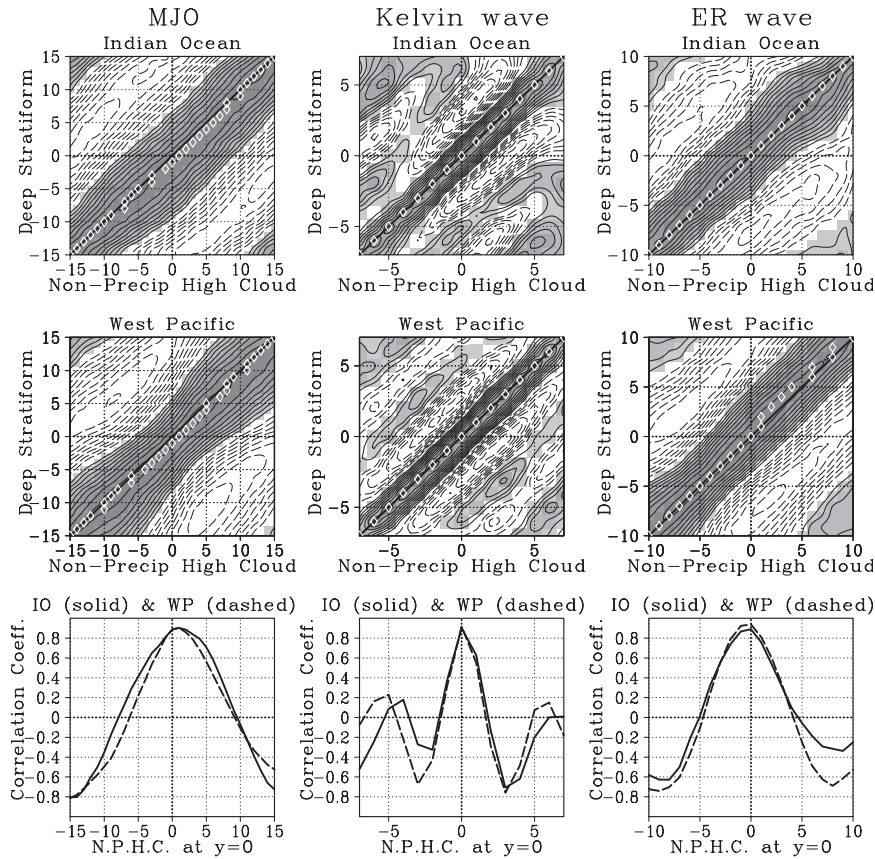
Fig. 10.   Same as Fig. 4 but for the correlation between non-precipitating high cloud and deep stratiform coverages.

incoming shortwave flux (e.g., Flatau et al. 1997). This regulatory cycle is likely at work on intraseasonal time scales, but is perhaps much less efficient for a period typical of the Kelvin wave. The development of Kelvin wave convection therefore proceeds without the help of an external thermodynamic driver similar to the discharge-recharge mechanism proposed to explain the MJO periodicity (Bladé and Hartmann 1993).

The Kelvin wave dynamics per se does not favor the cooperation between convective heating and large-scale warming (Emanuel et al. 1994). The frictional moisture convergence, however, allows this cooperation to occur, so that the generation of eddy available potential energy prevents the Kelvin wave from damping (Wang and Rui 1990; Hendon and Salby 1994; Salby et al. 1994). The composite diagram indeed shows a moist anomaly centered on the equator to the east of the Kelvin wave convective peak (Fig. 2), led by moisture convergence by a day (Fig. 5). It is less obvious what gives rise to the off-equatorial wings of

moist anomaly (Fig. 2). Figure 11a shows boundary-layer (1000 hPa) wind and moisture convergence composited with respect to the Kelvin wave. The boundary wind field is overall as predicted by theories of the frictionally-modified Kelvin wave (cf., Salby et al. 1994; Moskowitz and Bretherton 2000), where anomalous wind is predominantly zonal but slightly tilted. There is no evident feature responsible for the off-equatorial moist anomaly in Fig. 11a. A possible mechanism accounting for the off-equatorial moist anomaly is a local enhancement of evaporation. There is however no supporting evidence for this possibility because neither SST anomaly (Fig. 2) nor near-surface wind anomaly (Fig. 11a) do not geographically match the observed CRH wings. Another potential mechanism is midtropospheric moisture convergence if the free troposphere has a relevant dynamics. This is actually feasible, as Fig. 11b reveals a mid-tropospheric (600 hPa) flow heading away from the equator near 0° in relative longitude. This poleward flow, likely a part
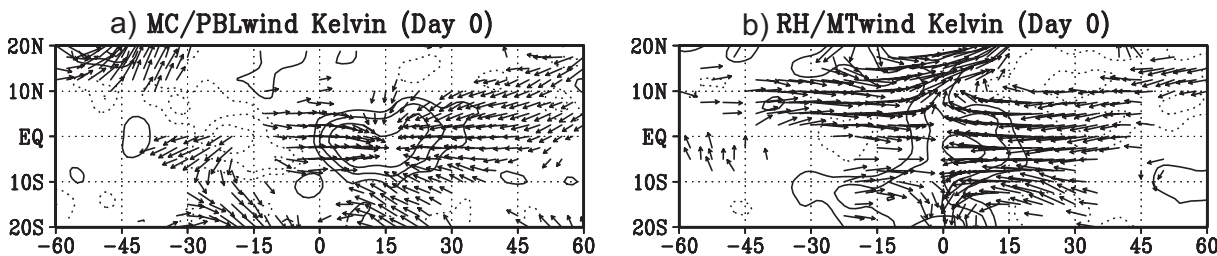
a) MC/PBLwind Kelvin (Day 0)

b) RH/MTwind Kelvin (Day 0)

Fig. 11.   Day-0 composite diagram for the Kelvin wave. *a*) 1000 hPa horizontal wind and moisture convergence contoured at every 1×10^{-5} kg m^{-2} s^{-1} with negative anomalies dashed. *b*) 600 hPa horizontal wind and CRH contoured at every 0.5% with negative anomalies dashed. The wind field is drawn only where the significance level is 95% or higher.
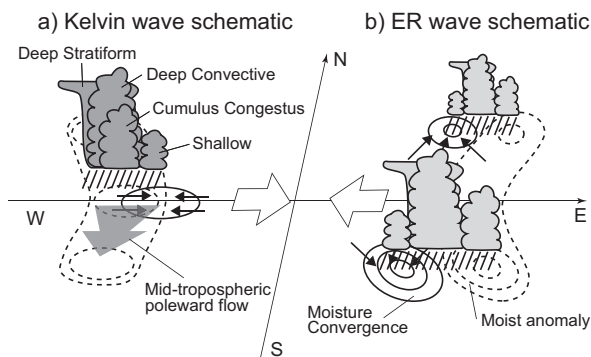
a) Kelvin wave schematic

b) ER wave schematic

Fig. 12. Schematic of (*a*) Kelvin wave and (*b*) ER wave. Solid and dashed contours represent moisture convergence and positive humidity anomaly, respectively. Black arrows denote convergent boundary-layer wind.

of the Rossby wave response to convective heating (Gill 1980), appears to converge into the off-equatorial humidity peak at 0° longitude and 20°S. The mid-tropospheric convergence presumably helps feed the off-equatorial moist anomaly with equatorial humid air. It is noted that while the Kelvin wave-composited wind structure is generally zonal in the lower troposphere, a vortical distortion has been often found in the upper-tropospheric wind field flanking the Kelvin wave convective peak (Nakazawa 1988; Takayabu and Murakami 1991; Masunaga 2007).

The off-equatorial moist anomaly is potentially ascribable to the extratropical origin. The gyre structure in Fig. 11b somewhat resembles a portion of the Rossby wave train in the subtropical jet initiating the Kelvin wave (Straub and Kiladis 2003a). Straub and Kiladis (2003a) presented observational evidence

suggesting that the subtropical jet in the southern hemisphere dynamically forces the Kelvin wave. Note that their analysis is focused on austral winter on the contrary to the current paper. Figure 2 of Straub and Kiladis (2003a) suggests that a single pair of gyres also emerge in the northern (or summer) hemisphere but only after Kelvin wave convection reaches the peak activity. As such, the summer hemispheric gyres accompanying the Kelvin wave, relevant to the southern hemispheric moist anomaly in the present analysis, is most likely viewed as the Rossby wave response as interpreted earlier. The northern counterpart of the off-equatorial moist anomaly, not discussed in this work, could be under the strong influence of extratropical disturbances.

For the Indian Ocean Kelvin wave (top-middle panel of Fig. 4), the correlation between moisture convergence and CRH abruptly rises along the ridge as the developing phase gives way to the decaying phase. In other words, the frictional moisture feedback works more efficiently for the waves emanating to the east of the convective peak than those coming in from the west. This may suggest that the Kelvin wave tends to grow in amplitude while passing over the Indian Ocean.

In summary, the progression of Kelvin wave convection and associated dynamic and thermodynamic environment are schematically illustrated in Fig. 12a. No discernible phase lag has been observed between different types of clouds except for a slight (< ~1 day) lead of shallow cumulus. The deepening of clouds toward the convective peak may have a role in releasing the boundary-layer moisture into the free troposphere (Straub and Kiladis 2002). The resultant increase in the mid-tropospheric humidity is speculated here to be transported poleward and moisten off-equatorial air. The fact that the Kelvin wave
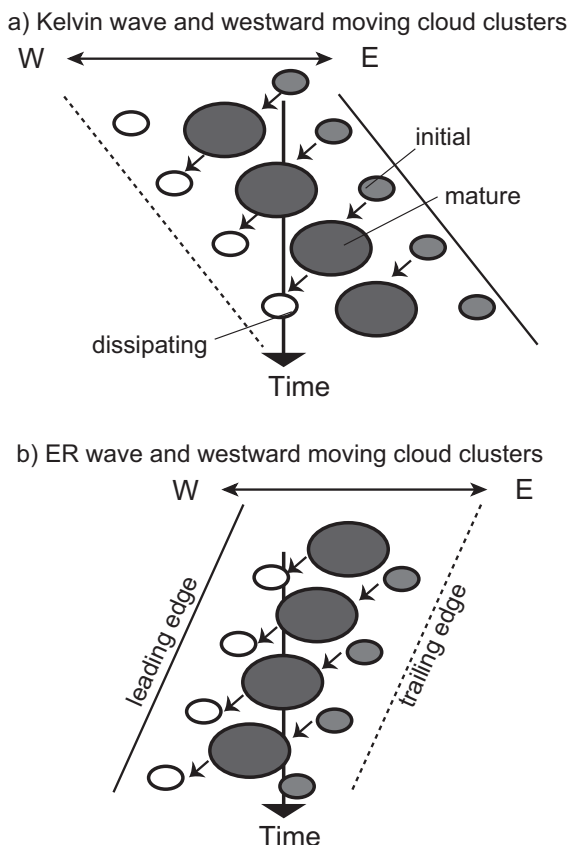
a) Kelvin wave and westward moving cloud clusters

b) ER wave and westward moving cloud clusters

Fig. 13.   Speculated configurations of cloud clusters embedded in (*a*) Kelvin wave and (*b*) ER wave. The Kelvin wave containing westward moving cloud clusters inside, as discovered by Nakazawa (1988), would experience the initial, mature, and dissipating stages of cloud clusters in this order when observed at a fixed location. Same cloud clusters within the ER wave envelope would result in the reverse life cycle when composited by a fixed point observation.

accompanies off-equatorial moist anomalies will be a key ingredient of the proposed MJO mechanism discussed in Section 5.3 below.

5.2   *Equatorial Rossby wave*

An intriguing feature regarding the ER wave is that a moist anomaly develops a day *after* deep stratiform coverage does (Fig. 6). Given that it takes 2 days for a moist anomaly to catch up with the preceding moisture convergence (Fig. 5), ER wave convection reaches its peak activity in between the moisture convergence and humidity maxima. Another result seemingly puzzling is that the deepening of convective clouds does not progress monotonically; shallow cumulus barely leads deep stratiform systems but cumulus congestus develops afterward (Fig. 8). A schematic of the ER wave structure is shown by Fig. 12b.

These behaviors peculiar to the ER wave might be understood in terms of the hierarchical structure of convectively coupled tropical disturbances. Synoptic-scale convective variability is known to involve finer-scale convective organization called cloud clusters (Nakazawa 1988). Nakazawa (1988) illustrated that cloud clusters migrate to the west while the envelope of cloud clusters or a super cloud cluster, likely coupled with the Kelvin wave, propagates eastward. It follows that an individual cloud cluster is initiated on the leading edge of the super cloud cluster and marches westward as it matures until it eventually dies out near the trailing edge. It is postulated here that the ER wave also has an embedded structure of cloud clusters moving to the west. The cloud clusters thus migrate in the same direction as the ER wave but at a faster speed. On the contrary to the Kelvin wave, cloud clusters should be initiated on the trailing edge of the ER wave and decay on the leading edge. An observer recording a temporal sequence of cloud clusters at a fixed point would report the reverse life cycle of cloud clusters during a passage of the ER wave (Fig. 13). It is very speculative but tempting to ascribe the observed lags of cumulus congestus and CRH to the composite convective progression traced backward in time. It is beyond the capacity of the current work to test this speculation and is left for future studies.

5.3   *Madden-Julian Oscillation*

It has been recognized in the literature that equatorial waves tend to be subject to a large-scale amplitude modulation within the MJO convective envelope (Dunkerton and Crum 1995; Straub and Kiladis 2003b; Masunaga et al. 2006). The MJO modulation of Kelvin wave packets is visually identifiable from time to time in Fig. 1, where notable examples are found in Jan–Feb 1999, Nov–Dec 2000, Jan–Feb 2001, and Jan–Feb 2004 among others. It is also seen in Fig. 1 that a ridge of the ER wave intersecting the MJO envelope occasionally accompanies convective burst. Some MJO events are not accompanied by Kelvin and ER wave packets within the convective envelope. Masunaga et al. (2006) discussed the hypothesis that the driver of MJO
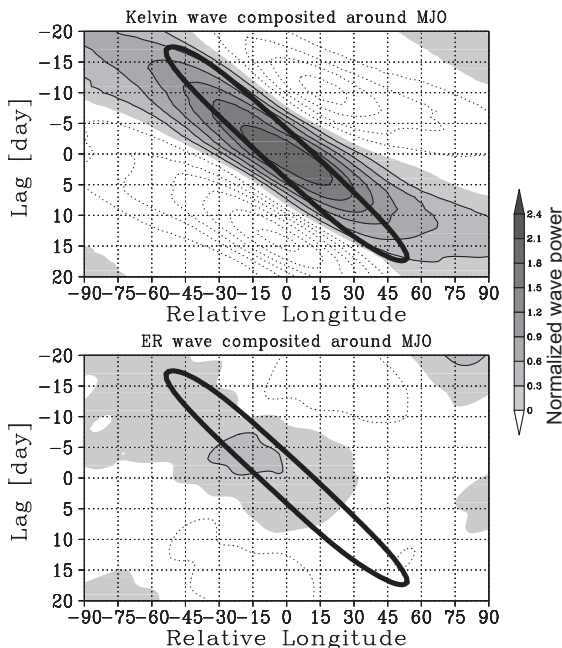
Fig. 14. The lag-longitude diagram of the Kelvin wave (*top*) and ER wave (*bottom*) composited with respect to the MJO convective peak. The compositing method is as described in Section 3. The power of Kelvin/ER wave-filtered deep stratiform coverage, normalized by the variance of each mode, is contoured at intervals of 0.3. Contours are dashed for negative anomalies. Positive anomalies are shaded. The MJO composited with respect to itself is drawn for reference by thick contour at twice the variance.

propagation in some cases might be a group of Kelvin wave packets dragging convective spots slowly to the east. In the hypothesis, the ER wave was speculated to contribute to the grouping of the wave packets by initiating and terminating Kelvin wave convection. Masunaga et al. (2006), however, did not demonstrate how the Kelvin wave could interact with the ER wave. In this closing section, an attempt is made to explore a possible mechanism of the wave interaction as inferred from the present findings.

Figure 14 shows the lag-longitude diagram of the Kelvin and ER waves composited with respect to the MJO convective peak. It is evident that the Kelvin wave is strongly modulated by the MJO. The Kelvin wave packet is slightly offset to the west (east) of the MJO envelope for negative (positive) lags, propagating

eastward as a whole somewhat faster than the MJO. It follows that the Kelvin wave approaches from the west before the MJO convective peak, while emanating to the east after the convective peak. In contrast, the MJO-composited ER wave shows little systematic pattern. The amplitude of the ER wave is therefore not affected much by changing MJO phases, as one may expect from Fig. 1. Nevertheless, the composite ER wave diagram shows a patch of weak positive anomaly loosely collocated with the area of the approaching Kelvin wave. Although it is not a primary driver of the MJO, the ER wave may act as a stochastic trigger fuelling MJO convection, activated when it intersects with the Kelvin wave.

It is noted that such systematic relationship between the MJO and the Kelvin and ER waves is not as clearly observed in OLR as in precipitation data. It is typically the case that OLR does not exhibit visible evidence of Kelvin and ER wave modulation while the modulation is clear in TRMM data for the same MJO event. OLR data, of course, captures the overall pattern of wave propagation, but noises from non-precipitating components such as cirrus clouds perhaps make it difficult to precisely trace the amplitude evolution and dissipation of convectively coupled waves. The composite analysis same as Fig. 14 but with OLR shows a qualitatively consistent result but is much noisier (Masunaga 2007).

Figure 15 is a schematic picture of the austral summer MJO, based on the results from the current analysis combined with general knowledge and the proposed hypothesis. A cycle of the MJO starts with the convective onset over the Indian Ocean. We have seen that a prior sea surface warming emerges as a distinct correlation maximum in the Indian Ocean (Fig. 4). A Kelvin wave packet emanating in response to the convective onset is accompanied by convective clouds moving eastward. Kelvin wave convection, however, ceases to be a critical component of the MJO once the MJO convective envelope leaves the Indian Ocean. While the convective onset in the Indian Ocean is initiated near the equator, the geographical center of deep stratiform coverage shifts away from the equator as MJO convection moves into the west Pacific (Fig. 16). The spatial maximum of deep stratiform coverage associated with the west Pacific MJO is located at 10°S, which is no longer explained by the Kelvin wave dynamics.

Figure 16 illustrates that the southeastward shift of the convective area occurs in parallel with the development of the horseshoe pattern of humidity
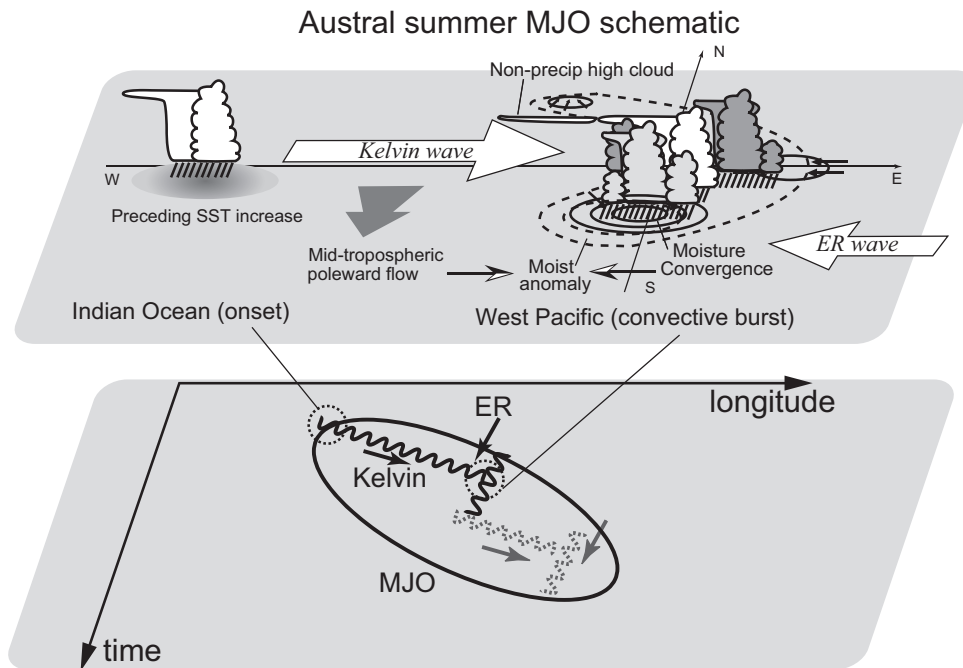
Austral summer MJO schematic

Fig. 15.   Same as Fig. 12 but for the MJO. The lower half shows the projection onto the time-longitude plane, constructed in combination with the hypothesis proposed by Masunaga et al. (2006).

anomaly. The equatorial tip of the horseshoe is likely ascribed to the frictional moisture convergence brought by the Kelvin wave. The both ends of the horseshoe requires another mechanism that transports moisture away from the equator. We discussed earlier that the mid-tropospheric convergence as a dynamical response to the Kelvin wave convective heating enables poleward moisture transport. The resulting off-equatorial spot of a high mid-tropospheric humidity would generate a condition favorable for organized convective systems to develop. It is conjectured that an MJO convective burst breaks out when an ER wave disturbance comes in the moist spot preconditioned by the Kelvin wave. As such, the spatial maximum in the MJO-composited moisture convergence (Fig. 2) is considered to originate from the ER wave dynamics. A moist anomaly is set up partly by the Kelvin wave mid-tropospheric flow before the arrival of the ER wave convergence. This perhaps explains why humidity does not lag or even leads moisture convergence for the MJO as we have seen in Fig. 5. The preceding moisture convergence lying around the equator is so subtle that it is unlikely important for the MJO. Meanwhile, the frictional moisture feedback is probably crucial for the propagation of the Kelvin wave

itself.

A schematic of the time-longitude section of the MJO is delineated in the lower half of Fig. 15. The MJO convective burst brought upon the arrival of the ER wave may be slightly pushed back to the east by the continuing propagation of the ER wave, or could stay for a while decoupled from the wave dynamics (Masunaga et al. 2006). The convective envelope resumes its eastward migration when another ridge of the Kelvin wave comes in. This whole process could occur at multiple times in a single MJO event. Masunaga et al. (2006) argued that the MJO convective envelope consists of a group of Kelvin wave packets and sporadic convective bursts triggered by intruding ER waves. In this theory, occasional interruptions of the Kelvin wave account for the slowness of MJO propagation. It is noted again that the hypothesis delineated here presumably explains aspects of major MJO events in austral summer but does not account for every case.

The convective progression associated with the MJO may be interpreted in part by superposing those with the Kelvin and ER waves. The MJO-composited shallow cumulus coverage (Fig. 2) resembles the horseshoe pattern, showing a prominent equatorial tip of the
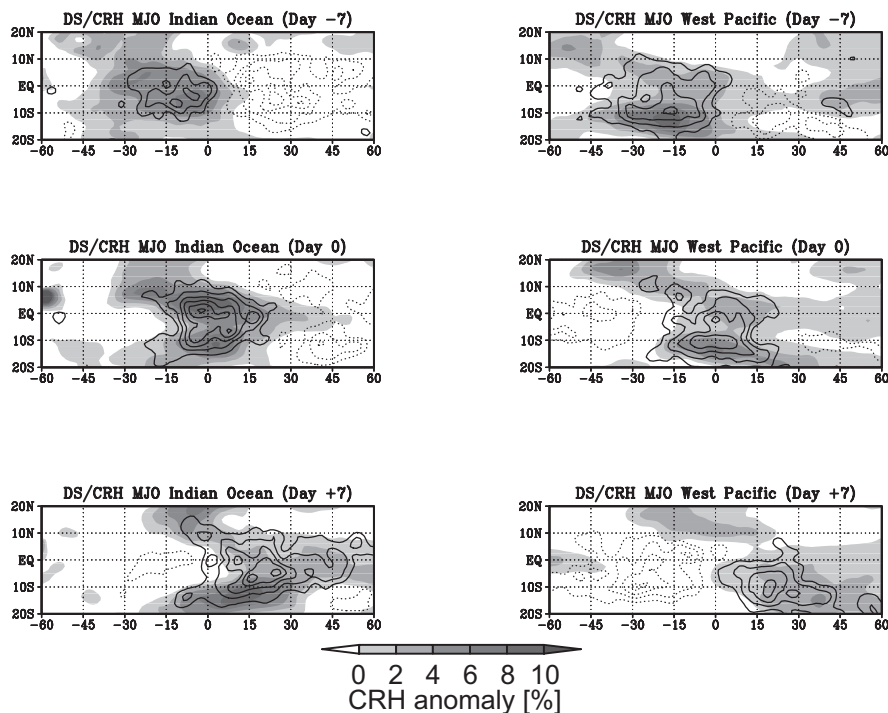
Fig. 16.   Lagged composite diagram for the Indian Ocean MJO (left) and west Pacific MJO (right). Deep stratiform coverage is contoured at intervals of 0.1% with negative anomalies dashed. CRH is shaded with negative anomalies omitted.

Kelvin wave origin. The convective progression starts with shallow cumulus ahead by ~1 day for the Kelvin wave, and so does it for the MJO (Fig. 7). On the other hand, composite cumulus congestus (not shown) exhibits an off-equatorial pattern more reminiscent of the ER wave (Fig. 16). Figure 8 shows that cumulus congestus lags deep stratiform systems for the ER wave while the former leads the latter for the MJO. It follows that cumulus congestus is observed on the eastern edge in both cases (Figs. 12 and 15), given that the ER wave propagates westward and the MJO migrates to the east.

Figure 10 implies that detrained cirrus lingers for about a day. Extensive cirrus clouds could have an important effect on the local thermodynamic cycle oscillating on an intraseasonal time scale. Radiative effects of high clouds may enhance the upper-tropospheric cooling (Hu and Randall 1994), promote the greenhouse effect (Stephens et al. 2004), or simply induce an energy transfer from the ocean to the atmosphere (Sobel and Gildor 2003). A locally regulated thermodynamic cycle would be a key that controls the MJO period (Bladé and Hartmann 1993), since the

interaction between the Kelvin and ER waves discussed above could explain the propagation of the MJO, but not its periodicity.

References

Benedict, J. J., and D. A. Randall, 2007: Observed characteristics of the MJO relative to maximum rainfall. *J. Atmos. Sci.*, **64**, 2332–2354.

Bladé, I., and D. L. Hartmann, 1993: Tropical intraseasonal oscillations in a simple nonlinear model. *J. Atmos. Sci.*, **50**, 2922–2939.

Bretherton, C., M. E. Peters, and L. E. Back, 2004: Relationships between water vapor path and precipitation over the trpical oceans. *J. Climate*, **17**, 1517–1528.

Cho, H.-K., K. P. Bowman, and G. R. North, 2004: Equatorial waves including the Madden-Julian Oscillation in TRMM rainfall and OLR data. *J. Climate*, **17**, 4387–4406.

Dunkerton, T. J., and F. X. Crum, 1995: Eastward propagating ~2- to 15-day equatorial convection and its relation to the tropical intraseasonal oscillation. *J. Geophys. Res.*, **100**, 25781–25790.

Emanuel, K. A., J. D. Neelin, and C. S. Bretherton, 1994: On large-scale circulations in convecting atmospheres. *Quart. J. Roy. Meteor. Soc.*, **120**, 1111–1143.

Flatau, M., P. J. Flatau, P. Phoebus, and P. P. Niiler, 1997: The feedback between equatorial convection and local radiative and evaporative processes: The implications for intraseasonal oscillations. *J. Atmos. Sci.*, **54**, 2373–2386.

Gill, A. E., 1980: Some simple solutions for heat-induced tropical circulation. *Quart. J. Roy. Meteor. Soc.*, **106**, 447–462.

Haertel, P. T., G. N. Kiladis, A. Denno, and T. M. Rickenbach, 2008: Vertical-mode decompositions of 2-day waves and the Madden-Julian Oscillation. *J. Atmos. Sci.*, **65**, 813–833.

Hendon, H. H., and M. L. Salby, 1994: The life cycle of the Madden-Julian Oscillation. *J. Atmos. Sci.*, **51**, 2225–2237.

Hendon, H. H., and J. Glick, 1997: Intraseasonal air-sea interaction in the tropical Indian and Pacific Oceans. *J. Climate*, **10**, 647–661.

Hu, Q., and D. A. Randall, 1994: Low-frequency oscillations in radiative-convective systems. *J. Atmos. Sci.*, **51**, 1089–1099.

Jones, C. D., and B. C. Weare, 1996: The role of low-level moisture convergence and ocean latent heat flux of the Madden-Julian Oscillation: An obsevational analysis using ISCCP data and ECMWF analyses. *J. Climate*, **9**, 3086–3104.

Kemball-Cook, S. R., and B. C. Weare, 2001: The onset of convection in the Madden-Julian Oscillation. *J. Climate*, **14**, 780–793.

Kiladis, G. N., K. H. Straub, and P. T. Haertel, 2005: Zonal and vertical structure of the Madden-Julian Oscillation. *J. Atmos. Sci.*, **62**, 2790–2809.

Lin, J., B. Mapes, M. Zhang, and M. Newman, 2004: Stratiform precipitation, vertical heating profiles, and the Madden-Julian Oscillation. *J. Atmos. Sci.*, **61**, 296–309.

Lin, X., and R. H. Johnson, 1996: Kinematic and thermodynamic characteristics of the flow over the western Pacific warm pool during TOGA COARE. *J. Atmos. Sci.*, **53**, 695–715.

Luo, Z., and W. B. Rossow, 2004: Characterizing tropical cirrus life cycle, evolution, and inter-action with upper-tropospheric water vapor using Lagrangian trajectory analysis of satellite observations. *J. Climate*, **17**, 4541–4563.

Madden, R. A., 1986: Seasonal variatoins of the 40-50 day oscillation in the tropics. *J Atmos. Sci.*, **43**, 3138–3158.

Madden, R. A., and P. R. Julian, 1972: Description of global-scale circulation cells in the tropics with a 40–50 day period. *J. Atmos. Sci.*, **29**, 1109–1123.

Maloney, E. D., and D. L. Hartmann, 1998: Frictional moisture convergence in a composite life cycle of the Madden-Julian Oscillation. *J. Climate*, **11**, 2387–2403.

Mapes, B., S. Tulich, J. Lin, and P. Zuidema, 2006: The mesoscale convection life cycle: Building block or prototype for large-scale tropical waves? *Dyn. Atmos. Oceans*, **42**, 3–29.

Masunaga, H., 2007: Seasonality and regionality of the Madden-Julian Oscillation, Kelvin wave, and equatorial Rossby wave. *J. Atmos. Sci.*, **64**, 4400–4416.

Masunaga, H., T. Iguchi, R. Oki, and M. Kachi, 2002: Comparison of rainfall products derived from TRMM Microwave Imager and Precipitation Radar. *J. Appl. Meteor.*, **41**, 849–862.

Masunaga, H., T. S. L'Ecuyer, and C. D. Kummerow, 2005: Variability in the characteristics of precipitation systems in the tropical Pacific. Part I: Spatial structure. *J. Climate*, **18**, 823–840.

Masunaga, H., and C. D. Kummerow, 2006: Observations of tropical precipitating clouds ranging from shallow to deep convective systems. *Geophys. Res. Lett.*, **33**, doi:10.1029/2006GL026547.

Masunaga, H., T. S. L'Ecuyer, and C. D. Kummerow, 2006: The Madden-Julian Oscillation recorded in early observations from the Tropical Rainfall Measuring Mission (TRMM). *J. Atmos. Sci.*, **63**, 2777–2794.

Matsuno, T., 1966: Quasi-geostrophic motions in the equatorial area. *J. Meteor. Soc. Japan*, **44**, 25–43.

Morita, J., Y. N. Takayabu, S. Shige, and Y. Kodama, 2006: Analysis of rainfall characteristics of the Madden-Julian Oscillation using TRMM satellite data. *Dyn. Atmos. Oceans*, **42**, 107–126.

Moskowitz, B. M., and C. S. Bretherton, 2000: An analysis of frictional feedback on a moist equatorial kelvin mode. *J. Atmos. Sci.*, **57**, 2188–2206.

Nakazawa, T., 1988: Tropical super clusters within intraseasonal variations over the western Pacific. *J. Meteor. Soc. Japan*, **66**, 823–839.

Nakazawa, T., 1995: Intraseasonal oscillations during the TOGA-COARE IOP. *J. Meteor. Soc. Japan*, **73**, 305–319.

Roundy, P. E., and W. M. Frank, 2004: A climatology of waves in the equatorial region. *J. Atmos. Sci.*, **61**, 2105–2132.

Salby, M. L., R. R. Garcia, and H. H. Hendon, 1994: Planetary-scale circulations in the presence of climatological and wave-induced heating. *J. Atmos. Sci.*, **51**, 2344–2367.

Short, D. A., and K. Nakamura, 2000: TRMM radar observations of shallow precipitation over the tropical oceans. *J. Climate*, **13**, 4107–4124.

Sobel, A. H., and H. Gildor, 2003: A simple time-dependent model of SST hot spots. *J. Climate*, **16**, 3978–3992.

Stephens, G. L., P. J. Webster, R. H. Johnson, R. Engelen, and T. S. L'Ecuyer, 2004: Observational evidence for the mutual regulation of the tropical hydrological cycle and tropical sea surface temperatures. *J. Climate*, **17**, 2213–2224.

Straub, K. H., and G. N. Kiladis, 2002: Observations of a convectively coupled Kelvin wave in the eastern Pacific ITCZ. *J. Atmos. Sci.*, **59**, 30–53.

Straub, K. H., and G. N. Kiladis, 2003a: Extratropical forcing of convectively coupled Kelvin waves during austral winter. *J. Atmos. Sci.*, **60**, 526–543.

Straub, K. H., and G. N. Kiladis, 2003b: Interactions between the boreal summer intraseasonal oscillation and higher-frequency tropical wave activity. *Mon. Wea. Rev.*, **131**, 945–960.

Takayabu, Y. N., 1994: Large-scale cloud disturbances associated with equatorial waves. Part I: Spectral features of the cloud disturbances. *J. Meteor. Soc. Japan*, **72**, 433–448.

Takayabu, Y. N., and M. Murakami, 1991: The structure of super cloud clusters observed in 1–20 June 1986 and their relationship to easterly wave. *J. Meteor. Soc. Japan*, **69**, 105–125.

Takayabu, Y. N., K.-M. Lau, and C.-S. Sui, 1996: Observation of a quasi-2-day wave during TOGA COARE. *Mon. Wea. Rev.*, **124**, 1892–1913.

Trenberth, K. E., and C. J. Guillemot, 1998: Evaluation of the atmospheric moisture and hydrological cycle in the NCEP/NCAR reanalyses. *Clim. Dyn.*, **14**, 213–231.

Wang, B., 1988: Dynamics of tropical low-frequency waves: An analysis of the moist Kelvin wave. *J. Atmos. Sci.*, **45**, 2051–2065.

Wang, B., and H. Rui, 1990: Dynamics of the coupled moist kelvin-rossby wave on an equatorial β plane. *J. Atmos. Sci.*, **47**, 397–413.

Wheeler, M., and G. N. Kiladis, 1999: Convectively coupled equatorial waves: analysis of clouds and temperature in the wavenumber-frequency domain. *J. Atmos. Sci.*, **56**, 374–399.

Wheeler, M., G. N. Kiladis, and P. J. Webster, 2000: Large-scale dynamical fields associated with convectively coupled equatorial waves. *J. Atmos. Sci.*, **57**, 613–640.

Wheeler, M., and K. M. Weickmann, 2001: Real-time monitoring and prediction of modes of coherent synoptic to intraseasonal tropical variability. *Mon. Wea. Rev.*, **129**, 2677–2694.

Xie, X., and B. Wang, 1996: Low-frequency equatorial waves in vertically sheared zonal flow, Part II: unstable waves. *J. Atmos. Sci.*, **53**, 3589–3605.

Zhang, C., 1996: Atmospheric intraseasonal variability at the surface in the tropical western pacific ocean. *J. Atmos. Sci.*, **53**, 739–758.